Floquet-engineered fidelity revivals in the PXP model

F. Perciavalle,* F. Plastina, and N. Lo Gullo
Dipartimento di Fisica, Università della Calabria, 87036 Arcavacata di Rende (CS), Italy
and Gruppo Collegato di Cosenza, INFN, 87036 Arcavacata di Rende, Cosenza, Calabria, Italy

(Received 6 February 2026; revised 16 July 2026; accepted 20 July 2026; published 3 August 2026)

We investigate the dynamics of the periodically driven PXP model and show how the interplay between spectral properties and initial states gives rise to distinct dynamical regimes, revealed by the pattern of the revivals. For Néel-ordered initial states, revivals follow distinct trajectories governed primarily by a dominant quasienergy spacing in the Floquet spectrum. Initial states interpolating between Néel and fully polarized configurations display hybrid dynamics, whose character can be tuned through their overlap with Floquet eigenstates by varying the driving parameters. This tunability also provides different pathways to avoid Floquet thermalization, highlighting how both the initial state and the driving protocol shape long-lived dynamics in driven quantum many-body systems.

DOI: 10.1103/nbr6-9jz2

I. INTRODUCTION

In recent years, controlling the dynamics of quantum matter has emerged as a highly active research field, driven by the advent of versatile and programmable quantum platforms [1–9]. Within this broad landscape, the study of thermalization in isolated quantum systems has attracted significant attention from both theoretical and experimental points of view [10–18]. A key concept in understanding thermalization is the eigenstate thermalization hypothesis (ETH) [10–12], which states that individual energy eigenstates of generic interacting systems exhibit thermal properties when taking the averages of local observables. While ETH successfully accounts for the behavior of typical systems, it may fail to capture certain nonergodic phenomena. Quantum systems such as those described by the PXP model [14,19–22] host quantum many-body scars (QMBSs) [21,23–32], which are atypical eigenstates characterized by anomalously low degree of entanglement and support persistent coherent revivals despite being embedded in an otherwise thermal spectrum.

In this context, periodic driving further enriches the phenomenology of interacting quantum systems by enabling coherent control beyond static Hamiltonian settings and offering a powerful tool to manipulate and stabilize nonergodic many-body dynamics. Systems with time-periodic Hamiltonians are naturally described within Floquet theory, where the stroboscopic evolution at integer multiples of the driving period is governed by an effective Floquet Hamiltonian [33–40]. This framework enables access to a variety of dynamical regimes, including nonergodic behavior, subharmonic responses, time-crystalline phases, and controlled revival dynamics, all of which can be tuned through the driving amplitude and frequency [22,41–48]. In this paper, we investigate the emergence of revivals in the driven PXP model and their relation to the Floquet spectrum. By analyzing the dynamics for different initial states, we show how the revival phenomenology evolves across the driving-parameter space. For the Néel state, revivals follow well-defined trajectories controlled by the Floquet quasienergy structure. By contrast, states interpolating between Néel and fully polarized configurations display tunable hybrid behavior, where the system continuously interpolates between distinct dynamical regimes depending on the value of the driving parameters.

Furthermore, we analyze thermalization under periodic driving and identify different mechanisms for avoiding Floquet thermalization depending on the initial state [49–53].

While authors of previous works have explored revival dynamics and, in some cases, mapped out regimes of enhanced revivals [22,44,53–55], here, we show how fidelity revivals propagate across the driving-parameter space, providing a physically intuitive picture of the underlying dynamics and linking them to the structure of the Floquet quasienergy spectrum. We further demonstrate that periodic driving enables continuous interpolation between distinct dynamical regimes, providing control over both the revival timescales and the resulting nonergodic behavior. This tunability also gives access to different mechanisms for avoiding Floquet thermalization. Altogether, our results provide a unified picture of long-lived coherent dynamics in driven scarred systems and establish a flexible framework for Floquet engineering across a broad range of initial states.

The remainder of the paper is organized as follows. In Sec. II, we introduce the driven PXP model and provide an overview of Floquet theory. In Sec. III, we explore the revival mechanism in the driving parameter space for a system initialized in the Néel state, whose spectral origin is investigated in Sec. IV. In Sec. V, we analyze the revival mechanism for initial states interpolating between the Néel and fully

*Contact author: fraperciavalle97@gmail.com

Published by the American Physical Society under the terms of the Creative Commons Attribution 4.0 International license. Further distribution of this work must maintain attribution to the author(s) and the published article's title, journal citation, and DOI.

polarized states, and in Sec. VI, we discuss their thermalization properties. Finally, in Sec. VII, we draw our conclusions and outline some perspectives arising from this work.

II. DRIVEN PXP MODEL AND FLOQUET THEORY

We consider a quantum spin chain composed of L qubits described by a periodically driven PXP model with open boundary conditions (OBCs), whose Hamiltonian reads

$$\begin{aligned}\hat{H}(t) &= \frac{\Omega}{2}\hat{H}_{\mathrm{PXP}} - V(t)\hat{N},\\ \hat{H}_{\mathrm{PXP}} &= \hat{X}_1\hat{P}_2 + \sum_{j=2}^{L-1}\hat{P}_{j-1}\hat{X}_j\hat{P}_{j+1} + \hat{P}_{L-1}\hat{X}_L,\\ V(t)\hat{N} &= h\sin(\omega_d t)\sum_{j=1}^{L}\hat{N}_j = h\sin(\omega_d t)\sum_{j=1}^{L}\frac{1}{2}(\hat{\mathbb{1}}_j + \hat{Z}_j),\end{aligned} \tag{1}$$

where $\hat{Z}_j = |1\rangle_j\langle 1| - |0\rangle_j\langle 0|$ is the z-Pauli matrix, $\hat{X}_j = |1\rangle_j\langle 0| + |0\rangle_j\langle 1|$ is the x-Pauli matrix, $\hat{P}_j = \frac{1}{2}(\hat{\mathbb{1}}_j - \hat{Z}_j)$ is the projector onto the state $|0\rangle_j$, while $\hat{N}_j = |1\rangle_j\langle 1|$. In the following, we denote the remaining Pauli matrix as $\hat{Y}_j$. The parameters h and ω_d are the driving amplitude and frequency, respectively, while L denotes the system size. Throughout this work, we set $\hbar = 1$, and measure energy (and time) in units of Ω (and Ω^{-1}).

The PXP model naturally arises in systems of interacting Rydberg atoms operating in the blockade regime [13,14,19–21,32,56]. The periodic driving term can be experimentally implemented through a time-dependent detuning [22,41–44]. In the absence of driving, the PXP model exhibits a rich dynamical phenomenology characterized by a sensitive dependence on the choice of the initial state. When initialized in the fully polarized state $|\mathbf{0}\rangle = |0000\ldots\rangle$, the system rapidly explores the available Hilbert space and displays ergodic behavior consistent with the ETH [14]. By contrast, initialization in the Néel state $|\mathbb{Z}_2\rangle = |1010\ldots\rangle$ leads to a pronounced violation of ETH and to long-lived quantum revivals [14]. These revivals originate from the overlap of the Néel state with a set of atypical many-body eigenstates, interspersed within the remaining thermal-like spectrum, known as QMBS, which are responsible for coherent oscillatory dynamics. Beyond the polarized and Néel states, the PXP model supports broader classes of nonergodic initial configurations, including the family of so-called local reminiscent states, which retain long-time memory of their local structure [30]. The inclusion of a periodic drive further enriches the variety of dynamical behaviors of the PXP model, giving rise to phenomena such as subharmonic responses and enhanced fidelity revivals in specific parameter regimes [22,41–44,54].

In general terms, a periodically driven quantum system with Hamiltonian satisfying $\hat{H}(t) = \hat{H}(t+T)$, where $T = 2\pi/\omega_d$, can be analyzed within the framework of Floquet theory [33,34,39,57]. The time evolution operator $\hat{\mathcal{U}}(t,0) = \mathcal{T}\exp[-i\int_0^t dt'\,\hat{H}(t')]$can be expressed in terms of repeated applications of the single-period one $\hat{\mathcal{U}}(t+nT,0) = \hat{\mathcal{U}}(t,0)[\hat{\mathcal{U}}(T,0)]^n$ so that, at stroboscopic times $t = nT$, the dynamics are fully governed by the Floquet operator $\hat{\mathcal{U}}(T,0)$. A generic time-evolved state at stroboscopic times can be written as

$$|\psi(nT)\rangle = \sum_m c_m e^{-i\epsilon_m^F nT}\left|\epsilon_m^F\right\rangle, \quad c_m = \left\langle\epsilon_m^F\middle|\psi(0)\right\rangle, \tag{2}$$

where $|\epsilon_m^F\rangle$ denote the Floquet eigenstates of the single-period evolution operator, and $\lambda_m^F = e^{-i\epsilon_m^F T}$ are the corresponding eigenvalues. The quantities ϵ_m^F are referred to as quasienergies and are defined modulo $\omega_d = 2\pi/T$ since $\exp[-i(\epsilon_m^F + \omega_d)T] = \exp(-i\epsilon_m^F T)$. As a consequence, quasienergies are restricted to the Floquet Brillouin zone (FBZ) $\epsilon_m^F \in (-\omega_d/2, \omega_d/2]$. The structure of the Floquet spectrum therefore plays a central role in determining the long-time dynamics of the system and naturally motivates the definition of a Floquet Hamiltonian $\hat{H}^F$, implicitly defined through $\hat{\mathcal{U}}(T,0) = \exp(-i\hat{H}^F T)$.

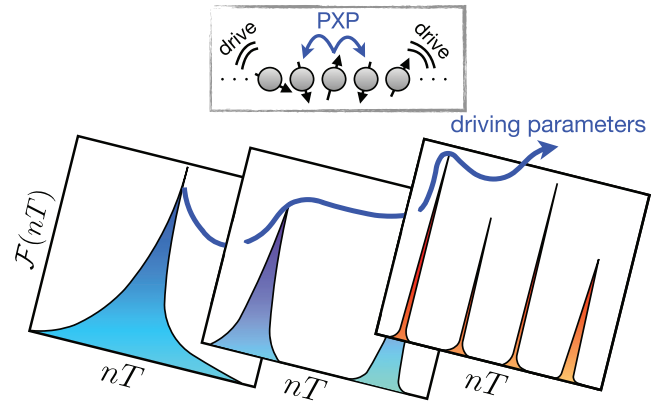


FIG. 1. Sketch of the periodically driven PXP model and of the resulting revival dynamics across the driving-parameter space. For Néel initial states, revivals follow well-defined trajectories controlled by the driving parameters. Other initial states can instead interpolate between distinct dynamical regimes, as illustrated by the blue arrow.

Periodic driving can thus be viewed as an effective tool to engineer renormalized Hamiltonians and access dynamical regimes that are difficult to realize in static settings. For the driven PXP model, it has been shown that, in suitable perturbative regimes, the effective Floquet Hamiltonian can be expressed as a mixture of PXP and PYP terms, see Appendix A [42]

$$\hat{H}^F = -\frac{\Omega}{2}J_0\left(\frac{h}{\omega_d}\right)\left[\cos\left(\frac{h}{\omega_d}\right)\hat{H}_{\mathrm{PXP}} - \sin\left(\frac{h}{\omega_d}\right)\hat{H}_{\mathrm{PYP}}\right]; \tag{3}$$

the relative importance of these contributions is controlled by the ratio h/ω_d, which sets the characteristic energy scale of the Floquet quasienergies. The effective Hamiltonian scales as $J_0(h/\omega_d)$ [42], where J_0 denotes the Bessel function of the first kind of order zero.

In the following, we will be interested in shedding light on the mechanism and conditions that regulate the emergence of quantum revivals in the driven PXP model, by tracking their trajectory in the driving parameter space, as sketched in Fig. 1. This analysis will provide insight into how the

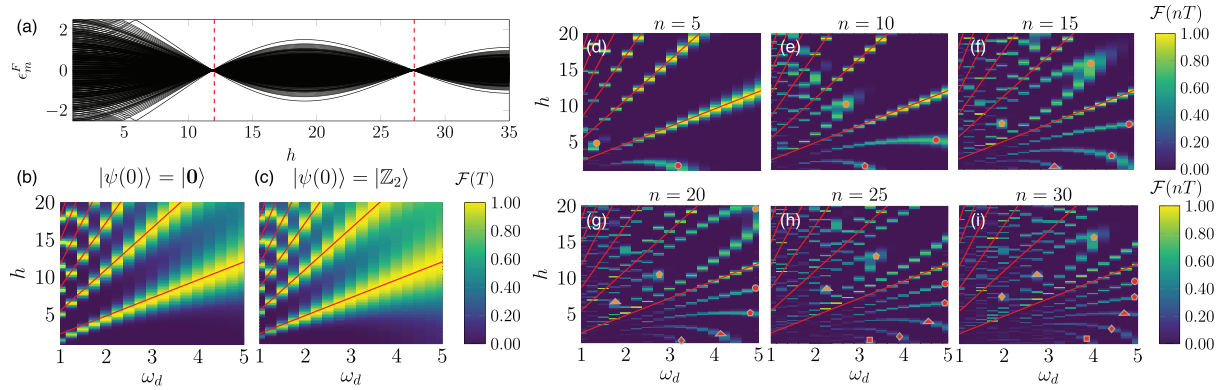


FIG. 2. (a) Floquet quasienergy spectrum as a function of the driving amplitude h, for fixed $\omega_d = 5$ and $L = 12$. The vertical dashed red lines mark the first two zeros of the Bessel function $J_0(h/\omega_d)$, at $h/\omega_d \approx 2.4048,\ 5.5201$. (b) and (c) One-period fidelity $\mathcal{F}(T)$ for the polarized $|\mathbf{0}\rangle$ and the Néel state $|\mathbb{Z}_2\rangle$, respectively, as a function of h and ω_d, with $L = 12$. Red lines indicate the zeros of $J_0(h/\omega_d)$. (d)–(i) Stroboscopic fidelity $\mathcal{F}(nT)$ for a system initialized in the Néel state, shown at different stroboscopic times nT (reported above each panel), with $L = 12$. The revival dynamics have the structure of a wave, propagating across the driving-parameter space, with the red and orange symbols tracking the trajectories of its crests in different regions separated by the zeros of $J_0(h/\omega_d)$. Explicitly, red symbols are used in the region $h/\omega_d < 2.4048$ and orange ones in the region $2.4048 < h/\omega_d < 5.5201$.

revival dynamics can be engineered and controlled through the driving protocol.

III. REVIVAL MECHANISM IN THE DRIVEN PXP MODEL

In this section, we investigate the stroboscopic dynamics generated by the Floquet operator and relate the emergence of fidelity revivals to the structure of the Floquet spectrum. This analysis reveals how the revival dynamics evolve across the driving-parameter space.

The first step is a careful analysis of the Floquet spectrum as a function of the driving parameters. According to Ref. [42], in the high-amplitude and high-frequency regime, $\hat{H}^F$ can be effectively described as a combination of the PXP and PYP models, modulated by the factor $J_0(h/\omega_d)$, except at the zeros of this function $h/\omega_d \approx 2.4048,\ 5.5201,\ \ldots$. In Fig. 2(a), we show the Floquet quasienergy spectrum as a function of the driving amplitude h, for fixed $\omega_d = 5$ and $L = 12$. The spectrum exhibits a characteristic candylike structure, with a bandwidth that approximately follows $|J_0(h/\omega_d)|$, in good agreement with the spectrum of the effective Floquet Hamiltonian (see Appendix A). For h smaller than ω_d, the quasienergies spread over the full FBZ $(-\omega_d/2, \omega_d/2]$. Near the zeros of $J_0(h/\omega_d)$, however, the spectrum narrows significantly, while retaining a finite bandwidth, while the spectrum of the effective Hamiltonian squeezes to zero bandwidth. We refer to these regions, where the bandwidth of $\hat{H}^F$ vanishes, as Floquet spectrum narrowing (FSN) regions. As we show below, the FSN plays a key role in shaping the revival dynamics and the emergence of long-lived coherent behavior in the driven system. The dependence of the Floquet spectrum on the system size L is discussed in Appendix B. To explore this mechanism, we follow the stroboscopic fidelity

$$\mathcal{F}(nT) = |\langle\psi(nT)|\psi(0)\rangle|^2, \tag{4}$$

which quantifies the similarity between the initial state and the time-evolved state at stroboscopic times. It serves as a powerful tool to probe the periodic dynamics of the system. By analyzing the time evolution at stroboscopic times, we can capture the key features that lead to the emergence of revivals and gain insight into the conditions that govern their appearance.

Let us focus on $n = 1$ first. Figures 2(b) and 2(c) show $\mathcal{F}(T)$, the single-period memory loss, for the polarized $|\mathbf{0}\rangle$ and Néel $|\mathbb{Z}_2\rangle$ states at $L = 12$. Memory loss is largest near the FSN region, negligible for $h/\omega_d < 2.4048$, and partial at high driving amplitude/frequency, with the Néel state generally preserving memory better.

We now move on to discuss the revival mechanism, quantified by the n-period fidelity $\mathcal{F}(nT)$, a quantity that measures the recurrence of the initial state at stroboscopic times and captures the memory degradation over intervals of nT. This can be understood by noting that $\hat{\mathcal{U}}(nT, 0) = [\hat{\mathcal{U}}(T, 0)]^n$, so that $|\langle\psi[(n+k)T]|\psi(kT)\rangle|^2 = |\langle\psi(nT)|\psi(0)\rangle|^2 = \mathcal{F}(nT)$, showing that the stroboscopic fidelity generally provides a measure of memory degradation over time intervals separated by nT, capturing how well the system retains its initial configuration across stroboscopic periods.

Figures 2(d)–2(i) show the evolution of $\mathcal{F}(nT)$ at stroboscopic times for a system initialized in the Néel state, revealing a propagation mechanism for the revival dynamics. In the FSN regions, marked by the red lines, the dynamics are strongly slowed down due to the compression of the Floquet bandwidth. Away from these regions, revivals first emerge at small driving amplitudes and progressively move across the driving-parameter space as time evolves. This behavior resembles a wave propagating in the (h, ω_d) plane, with the FSN regions acting as dynamical barriers that strongly hinder the propagation at short times. At longer times, however, the dynamics gradually penetrate these regions and revivals develop over broader portions of parameter space.

In Fig. 2, we focus on the regions $h/\omega_d < 2.4048$ and $2.4048 < h/\omega_d < 5.5201$. The red and orange symbols track the corresponding revival trajectories and highlight how the revival peaks spread across parameter space. This propagation

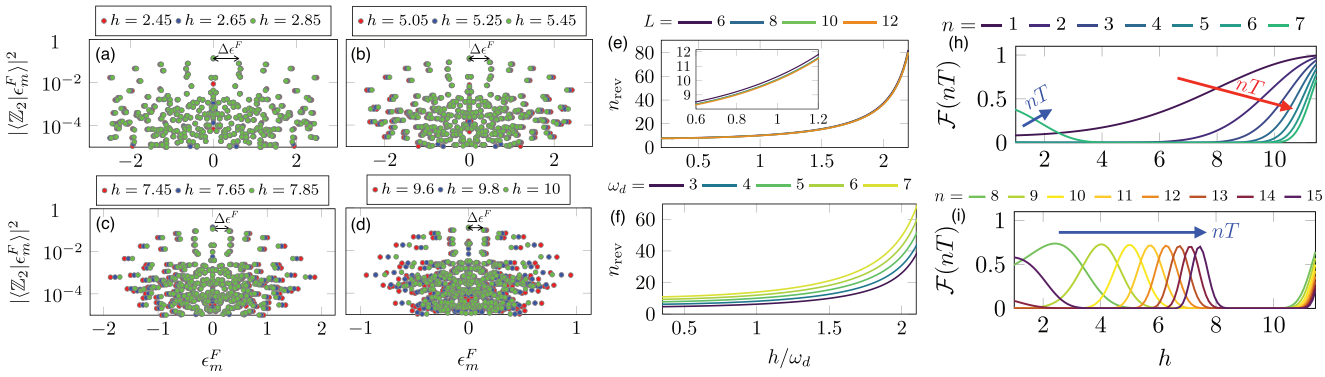


FIG. 3. Spectral properties and revival dynamics of the Néel state in the regions of $h/\omega_d < 2.4048$. (a)–(d) Overlap between the Néel state and the Floquet eigenstates for different driving amplitudes h, with $\omega_d = 5$ and $L = 12$. The dominant quasienergy spacing $\Delta\epsilon^F$ is highlighted in each panel. (e) and (f) Revival time n_{rev}, with $T_{\text{rev}} = 2\pi/\Delta\epsilon^F$, as a function of h/ω_d. Panel (e) shows the dependence on the system size L at fixed $\omega_d = 5$ (with the inset showing a zoom of the same quantity), while panel (f) reports the dependence on ω_d for fixed $L = 10$. (h) and (i) Stroboscopic fidelity $\mathcal{F}(nT)$ as a function of h for a system initialized in the Néel state, with $L = 12$ and $\omega_d = 5$. Panel (h) corresponds to the decay regime ($n \leqslant 7$), while panel (i) shows the revival regime ($8 \leqslant n \leqslant 15$). The arrows are intended to guide the eye by indicating the propagation of the revival peaks across the driving-parameter space.

mechanism provides a direct route for controlling the revival times through the driving parameters. As we discuss below, it originates from the deformation of the Floquet spectrum and from the changing overlap between the Néel state and the Floquet eigenstates.

In the figure, we focus on the regions $h/\omega_d < 2.4048$ and $2.4048 < h/\omega_d < 5.5201$. To highlight the propagation of the revivals, we mark the wave crests with orange and red symbols, which track the evolution both in time and across this fictitious parameter space. This representation illustrates how the revivals emerge in the small h region of parameter space and then spread, providing a visual and quantitative understanding of the dynamics underlying the stroboscopic memory and revival behavior in the driven PXP system. The presence of this highly controllable mechanism is intriguing, as it allows us to tune the parameters to determine, on demand, the specific times at which revivals occur. This behavior can be understood in terms of the deformation of the Floquet spectrum induced by tuning the driving parameters, particularly through changes in its overlap with the Néel state.

IV. SPECTRAL ORIGIN OF THE REVIVAL MECHANISM

In this section, we discuss the properties of the Floquet spectrum, focusing on the overlaps with the Néel state and provide a quantitative explanation of the revival behavior, linking the observed dynamics directly to the spectral structure of the system. In Figs. 3(a)–3(d), we show the overlaps of the Néel state with the Floquet spectrum across four distinct regions of the driving amplitude at fixed $\omega_d = 5$. The four regimes considered correspond to the following ranges of driving amplitudes: small ($h \in [2.45, 2.85]$), moderate ($h \in [5.05, 5.45]$), high ($h \in [7.45, 7.85]$), and very high ($h \in [9.6, 10]$), close to the FSN.

Despite their differences, these regimes share a common structure: an arc of dominant states, reminiscent of the QMBS in the undriven model, with the remaining states forming the bulk. This separation becomes more pronounced as the driving amplitude h approaches the FSN. States on the arc exhibit spacings that depend on h: Increasing h reduces the Floquet bandwidth and overall spacing, with edge states being more sensitive than central ones. We identify the Floquet energy separation $\Delta\epsilon^F$ between the zero-quasienergy state and its nearest neighbor on the arc as the dominant energy scale [see Figs. 3(a)–3(d)], which approximates the energy spacing between neighboring arc states far from the FSN and remains relevant near the FSN, despite the overlap reduces when approaching the edges.

One can expect the latter energy scale to determine the time at which revivals occur. Thus, we define $T_{\text{rev}} := 2\pi/\Delta\epsilon^F$ and introduce

$$n_{\text{rev}} = \frac{T_{\text{rev}}}{T} := \frac{\omega_d}{\Delta\epsilon^F}, \tag{5}$$

which specifies the multiples of the driving period at which revivals are expected to appear. In Figs. 3(e) and 3(f), we report the behavior of n_{rev} as a function of h/ω_d for different system sizes L, with $\omega_d = 5$ [panel (e)], and for different values of ω_d, with $L = 10$ [panel (f)]. The behavior of n_{rev} is well fitted by $n_{\text{rev}} = \frac{\omega_d}{\gamma J_0(h/\omega_d)} + \alpha$, where the fit parameters γ and α depend on ω_d (see Appendix C). For h/ω_d approaching the first zero of the Bessel function, we find $n_{\text{rev}} \approx \frac{\omega_d}{\gamma J_0(h/\omega_d)}$, indicating that $\Delta\epsilon^F \propto J_0(h/\omega_d)$. This shows that the reduction of the dominant level spacing follows the compression of the entire Floquet bandwidth, providing a useful tool for understanding the revival mechanism.

Having the Floquet spectral structure of the system in mind, we now discuss the evolution of $\mathcal{F}(nT)$ at fixed ω_d, as shown in Figs. 3(h) and 3(i) for $h < 2.4048\omega_d$. We identify two distinct phases: the decay phase [panel (h)], where the fidelity steadily decreases, and the revival phase [panel (i)], where the fidelity exhibits characteristic revival peaks. In the decay phase, $\mathcal{F}(nT)$ gradually decreases, forming a bell-like structure around the FSN, where dynamics are slow. In the revival phase, sharp fidelity peaks signal the return of the system state, following the mechanism illustrated in Fig. 2. The first

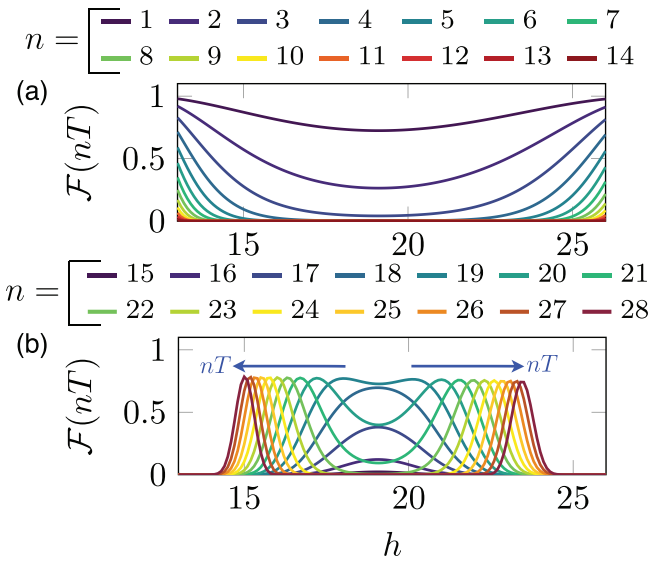


FIG. 4. Revival mechanism in the region of h/ω_d in between the two zeros of $J_0(h/\omega_d)$: $2.4048 < h/\omega_d < 5.5201$. We consider $\omega_d = 5$ and $L = 12$. Panel (a) shows the decay regime, characterized by a monotonic decrease of the fidelity. Panel (b) shows the revival regime, where the revival peaks propagate across the driving amplitude h, as highlighted by the blue arrows.

significant revival appears at $n = 8$ for small h, with a broad distribution that shifts toward the FSN and narrows over time. This shift occurs because $\Delta\epsilon^F$ decreases with increasing h, while the narrowing reflects the varying sensitivity of the spectrum to h: Weakly sensitive regions produce revivals over a wide h range, whereas highly sensitive regions near the FSN restrict the range. Such features provide a handle for controlling the timing of revivals: Broader distributions allow flexible tuning of h, while narrower distributions require precise calibration. By $t = 15T$, an emergent tail at small h indicates the onset of second revivals.

Some slight modifications occurs to revival mechanism in the region $2.4048 < h/\omega_d < 5.5201$ at fixed ω_d [see Figs. 4(a) and 4(b)]. Here, the decay phase persists longer, with no significant revival before roughly twice the minimal revival time observed previously, indicating a slower initial relaxation. In the revival phase, a blob forms at the center of the h interval, grows to its maximum height, then splits into two parts, which move symmetrically toward the FSN regions, while narrowing over time. This behavior reflects the symmetric response of different Floquet spectrum regions and the progressive constraint imposed by the FSN. For $t \leqslant 28T$, no second revivals occur, consistent with a slowing down of the dynamics, caused by the reduced Floquet bandwidth across regions separated by the FSN [Fig. 2(a)].

V. REVIVAL MECHANISM INTERPOLATING BETWEEN POLARIZED AND NÉEL STATES

In this section, we investigate how the revival mechanism depends on the choice of initial state. Specifically, we track the evolution of the mechanism by interpolating between the polarized and Néel states using the $|\Theta_+\rangle$ state

$$|\Theta_+\rangle = |\theta_+\rangle \otimes |0\rangle \otimes |\theta_+\rangle \otimes |0\rangle \otimes \ldots, \tag{6}$$

where $|\theta_+\rangle := \cos(\theta)\,|0\rangle + \sin(\theta)\,|1\rangle$. By varying θ in the interval $[0, \pi/2]$, the state smoothly interpolates between the polarized state $|\mathbf{0}\rangle = |0000\ldots\rangle$ and the Néel state $|\mathbb{Z}_2\rangle = |1010\ldots\rangle$. We perform our analysis by fixing ω_d.

We begin by analyzing the overlap of the initial state with the Floquet spectrum. Fixing h, we study how the overlap structure evolves for different values of $\theta \in [0, \pi/2]$, see Fig. 5(a). For small θ, the overlap predominantly reflects a bulklike configuration in line with that of a polarized state. As θ increases, the structure gradually evolves, exhibiting the characteristic arc of nearly equally spaced states seen above the bulk in the case of the Néel state. This similarity can be visually appreciated by comparing the emergent arc in these plots, highlighted with a black dashed line, to the reference arc of the Néel state, shown in gray, with the black arc gradually converging toward the gray one as θ approaches $\pi/2$.

We analyze the stroboscopic fidelity at $t = 10T$ for $h < 2.4048\,\omega_d$ [Fig. 5(b)]. For small θ, fidelity is low with shallow humps due to finite-size effects, indicating incomplete ergodicity. As θ increases, a central peak emerges from Floquet arc formation, signaling revivals, and reaches a maximum at $\theta = \pi/2$ (Néel state). Intermediate θ shows long tails at small h, reflecting moderate memory over a broad range, whereas the limits ($\theta = 0, \pi/2$) yield either weak or highly localized fidelity.

Next, we focus on the intermediate case $\theta = \pi/4$ to investigate the effect of varying h on both the Floquet spectrum and dynamics. The overlap of $|\Theta_+(\pi/4)\rangle$ with Floquet eigenstates is shown in Fig. 5(c). Unlike the Néel state, whose overlap structure remains largely insensitive to h [see Figs. 3(a)–3(d)], the intermediate-θ state exhibits a strong h dependence, indicating access to qualitatively distinct spectral and dynamical regimes. At small h, the overlap displays an approximately exponentially growing pattern, with a set of isolated low-quasienergy states occupying the top-left region of the plot. Remarkably, as h approaches the FSN, the overlap recovers a Néel-like configuration, demonstrating that, at intermediate θ, tuning h allows exploration of two fundamentally different spectral structures. This is evident from the emergent correspondence between the arc patterns in these plots (black dashed line) and those of the Néel state (gray dashed line) which are reported as the reference. We note that, whereas in the case shown in Fig. 5(a), the correspondence emerges from the fact that θ interpolates between the polarized and Néel states, here, the result is less intuitive and more striking. It demonstrates that the driving parameters can be appropriately tuned to generate Néel-like dynamics even from different initial states.

To illustrate this, we fix $\theta = \pi/4$ and track the evolution of the revival peaks as a function of h, as shown in Fig. 5(d). Revival peaks emerge at small h and move toward the FSN while narrowing, resembling the Néel-state mechanism. At small h, dynamics are irregular due to a different overlap structure, becoming regular near the FSN. Thus, intermediate θ shows two coexisting behaviors: fluctuating dynamics at small h and structured revivals at larger h, reflecting distinct mechanisms for avoiding thermalization (Sec. VI) and linking

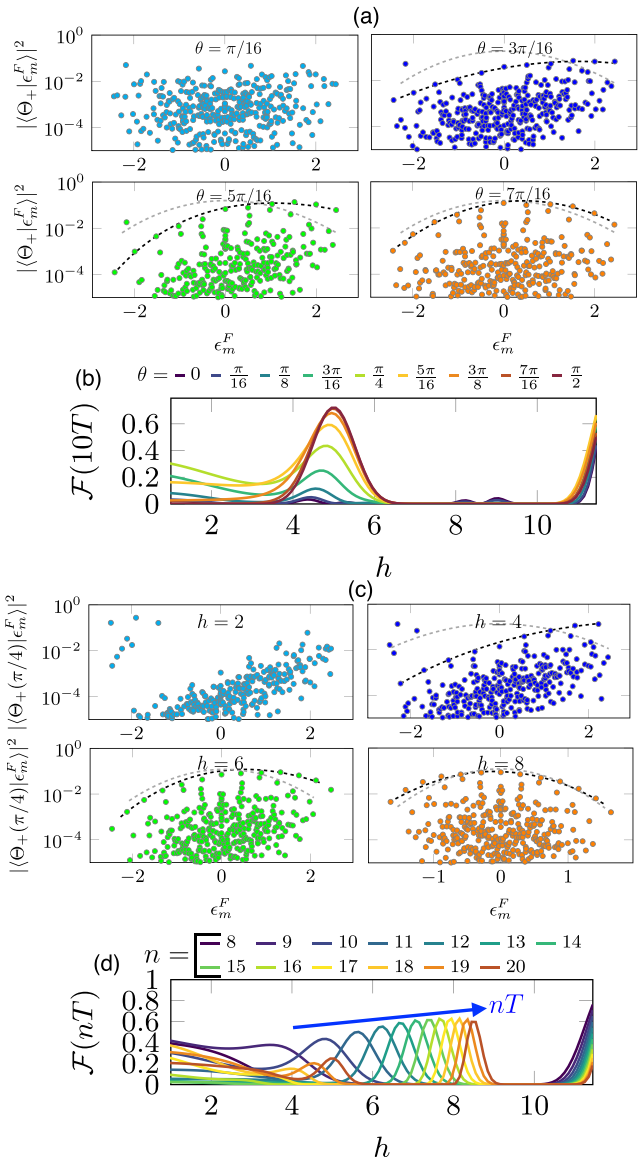


FIG. 5. Revival mechanism for the $|\Theta_+\rangle$ state with $\omega_d = 5$ and $L = 12$. (a) Overlap between the $|\Theta_+\rangle$ state and the Floquet eigenstates for different values of θ (different colors), computed at fixed $h = 5$. (b) Fidelity between the initial state $|\Theta_+\rangle$ and its stroboscopic time-evolved state at $t = 10T$, shown as a function of h for several values of θ in the range 0 to $\pi/2$. (c) Overlap between the $|\Theta_+\rangle$ state and the Floquet eigenstates for different values of h (different colors), computed at fixed $\theta = \pi/4$. (d) Fidelity for $\theta = \pi/4$ evaluated at different stroboscopic times nT, with n indicated in the legend. The blue arrow guides the eye along the time evolution of the revivals during the revival phase. In panels (a) and (c), the dashed black lines are guides to the eye highlighting the emergence of arclike structures, while the dashed gray line indicates the corresponding arc structure for the Néel-state case.

spectral deformation to the observed dynamics. Within the effective Floquet Hamiltonian picture discussed above, this evolution can be understood as a consequence of tuning h across the crossover between the PXP- and PYP-dominated regimes, with an intermediate region where the two contributions coexist and determine the observed dynamical behavior.

VI. NONTHERMAL FLOQUET DYNAMICS AND INITIAL STATE DEPENDENCE

In the previous sections, we have analyzed the revival dynamics of the driven PXP model initialized in the Néel state as well as for initial states interpolating between it and the fully polarized state. A natural question concerns the ergodic properties of this dynamics. To address it, we look at the long-time dynamics of the system and study thermalization at the level of a single site, which we treat as a subsystem, while the rest of the chain plays the role of an effective bath that may induce thermalization. Periodically driven quantum systems are expected to thermalize when the expectation values of local observables agree with those computed in the infinite-temperature state $\hat{\rho}^{\rm erg} = \hat{\mathbb{1}}_D/D$, where D denotes the Hilbert-space dimension [10,50–52,58,59]. In our case, the relevant ergodic state is instead identified as $\hat{\rho}^{\rm erg} = \hat{\mathbb{1}}_{F_{L+2}}/F_{L+2}$ since the dynamics are restricted to the blockaded subspace of dimension F_{L+2}.

To characterize the ergodic features of the dynamics, we quantify thermalization using the trace distance between the reduced density matrix of the subsystem and the corresponding ergodic state. We consider the following quantities:

$$\mathcal{D}\big[\hat{\rho}_S(t), \hat{\rho}_S^{\rm erg}\big] = \frac{1}{2}\big\|\hat{\rho}_S(t) - \hat{\rho}_S^{\rm erg}\big\|_1, \tag{7}$$

$$\mathcal{D}\big(\overline{\hat{\rho}_S(t)}, \hat{\rho}_S^{\rm erg}\big) = \frac{1}{2}\big\|\overline{\hat{\rho}_S(t)} - \hat{\rho}_S^{\rm erg}\big\|_1; \tag{8}$$

Here, $\hat{\rho}_S = {\rm Tr}_{\bar{S}}[\hat{\rho}]$, with $\bar{S}$ denoting the complement of S, and $\overline{\hat{\rho}_S(t)} = \frac{1}{t}\int_0^t dt' \hat{\rho}_S(t')$. These two quantities are employed to distinguish between strong and weak thermalization [60]. Strong thermalization occurs when both distances vanish at long times. If only the time-averaged distance vanishes while the instantaneous distance continues to oscillate, the system exhibits weak thermalization.

Focusing on the case where S is a single site, the trace distances reduce to distances between Bloch vectors associated with the corresponding single-site density matrices

$$\mathcal{D}\big[\hat{\rho}_j(t), \hat{\rho}_j^{\rm erg}\big] = \frac{1}{2}\big|\mathbf{r}_j(t) - \mathbf{r}_j^{\rm erg}\big|, \tag{9}$$

$$\mathcal{D}\big[\overline{\hat{\rho}_j(t)}, \hat{\rho}_j^{\rm erg}\big] = \frac{1}{2}\big|\overline{\mathbf{r}_j(t)} - \mathbf{r}_j^{\rm erg}\big|. \tag{10}$$

The Bloch vectors are given by $\mathbf{r}_j(t) = (\langle\hat{X}_j(t)\rangle, \langle\hat{Y}_j(t)\rangle, \langle\hat{Z}_j(t)\rangle)$, $\overline{\mathbf{r}_j(t)} = (\overline{\langle\hat{X}_j(t)\rangle}, \overline{\langle\hat{Y}_j(t)\rangle}, \overline{\langle\hat{Z}_j(t)\rangle})$, and $\mathbf{r}_j^{\rm erg} = (0, 0, Z_j^{\rm erg})$. The nonzero z component of the ergodic Bloch vector reflects the constraint imposed by the blockaded Hilbert space and is given by $Z_j^{\rm erg} = \frac{F_j F_{L-j+1} - F_{j+1}F_{L-j+2}}{F_{L+2}}$ (see Appendix D). Thus, the single-site thermalization passes through the convergence of local observables $\langle\hat{X}_j(t)\rangle, \langle\hat{Y}_j(t)\rangle, \langle\hat{Z}_j(t)\rangle$ and their time averages to, respectively, 0, 0, $Z_j^{\rm erg}$.

We begin by examining the thermal behavior of the system at the level of the entire chain. To this end, we define the spatially averaged observables $X(t) = \frac{1}{L}\sum_{j=1}^L \langle\hat{X}_j(t)\rangle$, $Y(t) = \frac{1}{L}\sum_{j=1}^L \langle\hat{Y}_j(t)\rangle$, and $Z(t) = \frac{1}{L}\sum_{j=1}^L \langle\hat{Z}_j(t)\rangle$. In Figs. 6(a) and 6(b), we show the time evolution of X and Z, while the dynamics of Y are reported in Appendix E. We fix $\omega_d = 5$, consider the regime $h < 2.4048\omega_d$, and focus on three rep-

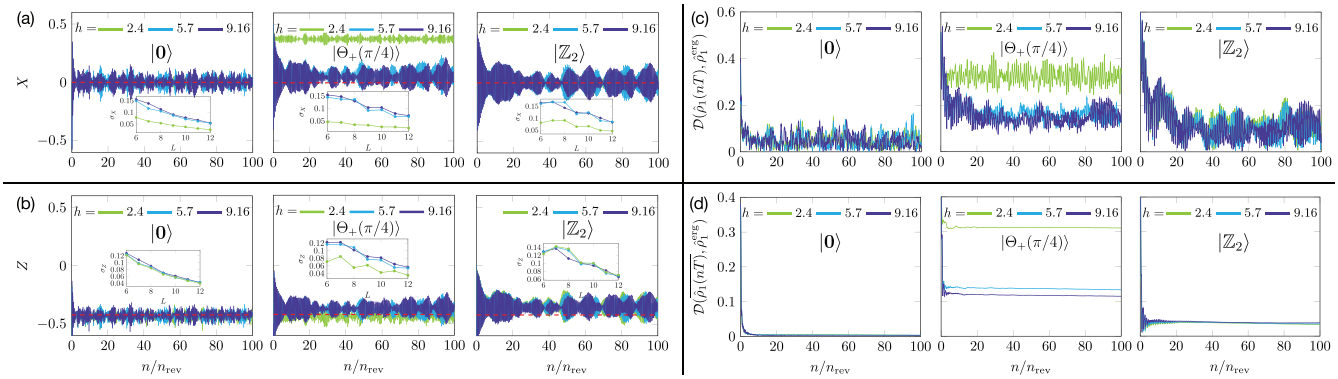


FIG. 6. Analysis of Floquet thermalization for different initial states $[|\mathbf{0}\rangle\,,\ |\Theta_+(\pi/4)\rangle\,,\ |\mathbb{Z}_2\rangle]$ and different driving amplitude values $h = 2.4, 5.7, 9.14$, showing revival times that are approximately integer multiples of the period $n_{\rm rev} = \omega_d/\Delta\epsilon^F \approx 8, 11, 25$. The driving frequency is fixed to $\omega_d = 5$ and $L = 12$. Dynamics at stroboscopic times of (a) $X(t)$ and (b) $Z(t)$ for the three initial states and the three values of the driving amplitude compared with their ergodic expectations $X^{\rm erg} = 0$ and $Z^{\rm erg}$ in dashed red. The insets report the standard deviations of the signals, defined as $\sigma_A = \sqrt{\frac{1}{100n_{\rm rev}}\sum_{n=1}^{100n_{\rm rev}}[A(nT) - \frac{1}{100n_{\rm rev}}\sum_{m=1}^{100n_{\rm rev}}A(mT)]^2}$, with $A = X, Z$. Panel (c) reports the trace distance between first-site density matrix at stroboscopic times $\hat{\rho}_1(nT)$ and the corresponding ergodic density matrix $\hat{\rho}_1^{\rm erg}$, while panel (d) reports the distance between the latter and the time-averaged first-site state $\overline{\hat{\rho}_1(nT)}$.

resentative values of h. These values are chosen such that $n_{\rm rev} = \omega_d/\Delta\epsilon^F$ is approximately an integer and correspond, respectively, to parameters far from the FSN ($h = 2.4$), at an intermediate location ($h = 5.7$), and close to ($h = 9.14$) the FSN.

We first examine X dynamics [Fig. 6(a)] for the three initial states. The polarized and Néel states are h independent: The polarized state fluctuates around the ergodic value $X^{\rm erg} = 0$, while the Néel state shows coherent revivals. In contrast, the interpolating state $|\Theta_+(\pi/4)\rangle$ is strongly h dependent, weakly fluctuating and far from ergodicity at small h, and approaching but not reaching the ergodic value at larger h, reflecting its h-dependent overlap with the Floquet spectrum. Here, Y dynamics show similar trends (Appendix E), with $h = 2.4$ and 5.7 producing similar behaviors. Here, Z dynamics [Fig. 6(b)] highlight ergodicity: The interpolating state consistently deviates from $Z^{\rm erg}$, the polarized state oscillates around it, and the Néel state clearly deviates even on average, indicating nonergodic behavior. The insets of Figs. 6(a) and 6(b) show the standard deviation of $X(nT)$ and $Z(nT)$ over $n \in [0, 100\,n_{\rm rev}]$ for different system sizes L. The polarized state exhibits a smooth decay with L, indicating thermalization in the thermodynamic limit, while the Néel and interpolating $|\Theta_+(\pi/4)\rangle$ states show irregular L dependence, reflecting persistent oscillations and preventing clear scaling. Overall, fluctuations are smaller away from the FSN, with $h = 2.4$ often showing the lowest values.

Finally, we analyze the instantaneous and time-averaged distances defined in Eqs. (9) and (10). For the instantaneous distance, the polarized state is the closest to the ergodic value, with small fluctuations due to the finite system size. Larger instantaneous distances are observed for the Néel and interpolating states. The interpolating state stays far from zero throughout the dynamics, never locally resembling the ergodic state. For h far from the FSN, this distance is especially large, reflecting a regime far from thermalization, due to the significant contributions of $X(t)$ and $Y(t)$. The time-averaged distance confirms these trends. The Néel and interpolating states avoid ergodicity in distinct ways, while the polarized state approaches the ergodic expectation on average. Although the finite system size prevents a sharp distinction between weak and strong thermalization, we can assert that the polarized state exhibits at least weak thermalization, whereas the other two states do not.

To conclude, two different forms of nonergodicity emerge. For the Néel state, the long-time-averaged local state has, on average, zero X and Y expectation values but a nonzero Z expectation value, causing it to deviate from the infinite-temperature prediction. For the interpolating state, particularly far from the FSN, the long-time-averaged state exhibits nonzero X and Y components, further enhancing the athermality of the system. This behavior is associated with a complex overlap structure with the Floquet states [Fig. 5(c)]. As the system approaches the FSN, the overlap structure of the interpolating state evolves toward an arclike pattern, and its long-time-averaged state becomes similar to that of the Néel state, with X and Y expectation values approaching zero on average yet remaining nonergodic.

VII. CONCLUSIONS AND OUTLOOK

We investigated the mechanism underlying the emergence of revivals in the nonergodic dynamics of the periodically driven PXP model through the stroboscopic evolution.

The Floquet quasienergy spectrum exhibits special regions of strong spectral compression, which we refer to as FSN regimes. In these regimes, the dynamics slow down substantially, strongly affecting the emergence and propagation of revivals from the Néel state. A clear physical picture emerges from the interplay between the revival dynamics and the Floquet spectral structure: Revivals propagate across the driving-parameter space, while the FSN regimes act as dynamical barriers that hinder their propagation. At the spectral level, the overlap structure between the Néel state and the Floquet eigenstates retains the characteristic arclike organization associated with scarred dynamics, while a dominant quasienergy spacing sets the characteristic revival timescale and regularity.

We then extended the analysis to initial states interpolating between the Néel and fully polarized configurations. Unlike the Néel state, these interpolating states exhibit a strong dependence on the driving parameters, allowing the dynamics to continuously evolve between distinct revival regimes. This behavior is directly reflected in the overlap structure with the Floquet eigenstates, which undergoes significant deformations under periodic driving. As a result, the driving can be used to engineer Néel-like revival dynamics even for states that would not display scarred behavior in the static case.

Finally, we investigated the long-time dynamics of the driven system to characterize Floquet thermalization. The fully polarized state exhibits weak thermalization at finite sizes, approaching the ergodic state on average. By contrast, the Néel state remains nonergodic, with long-time averages characterized by vanishing X and Y components but persistent nonthermal Z values. Interpolating states display a qualitatively different, hybrid behavior, developing finite long-time X and Y expectations and revealing alternative mechanisms for avoiding thermalization.

Overall, our results identify a controllable mechanism governing the emergence of revivals and preventing thermalization in the driven PXP model. The possibility of tuning the revival dynamics and the associated timescales through the driving parameters opens promising perspectives for controlling coherent many-body dynamics and stabilizing nonergodic behavior (e.g., for information storage).

Several directions naturally emerge from this work. It would be interesting to investigate the robustness of the revival mechanism under more general driving protocols, including quasiperiodic driving [42]. More broadly, periodic driving may provide a versatile framework for engineering and probing different forms of nonergodic dynamics, such as local reminiscent dynamics [30], which can be systematically investigated and tested under periodic driving.

ACKNOWLEDGMENTS

This work was partially funded by the PNRR MUR Project No. PE0000023-NQSTI through the secondary projects QuCADD, ThAnQ and QuSOE. Numerical simulations are performed by using the Julia package QUANTUMOPTICS.JL [61].

DATA AVAILABILITY

The data that support the findings of this article are not publicly available. The data are available from the authors upon reasonable request.

APPENDIX A: FLOQUET HAMILTONIAN AND COMPARISON WITH ORIGINAL DYNAMICS

In this Appendix, following Ref. [42], we briefly recall the Floquet Hamiltonian that accurately describes the periodically driven system and present numerical results demonstrating the agreement between the exact dynamics and the effective Floquet dynamics in the parameter regime considered in the main text. We also examine parameter choices for which this agreement breaks down. Defining $\tilde{\Omega} = \Omega/2$, in the high-frequency ($\omega_d \gg \tilde{\Omega}, h$) and high-amplitude ($h \gg \tilde{\Omega}$) regimes, where it can be derived using the Magnus expansion and Floquet perturbation theory, respectively, the Floquet Hamiltonian takes the form of a linear combination of the PXP and PYP Hamiltonians [42], with the latter obtained from the former by replacing each Pauli-x operator with a Pauli-y operator. Explicitly,

$$\hat{H}^F = -\frac{\Omega}{2} J_0\left(\frac{h}{\omega_d}\right)\left[\cos\left(\frac{h}{\omega_d}\right)\hat{H}_{\mathrm{PXP}} - \sin\left(\frac{h}{\omega_d}\right)\hat{H}_{\mathrm{PYP}}\right]; \tag{A1}$$

J_0 denotes the Bessel function of the first kind of order zero.

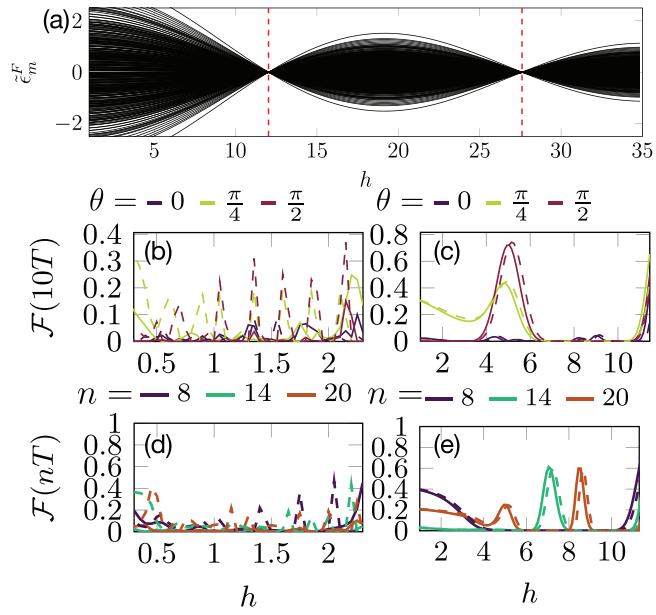


FIG. 7. (a) Spectrum of $\hat{H}^F$ as a function of h, with $L = 12$ and $\omega_d = 5$. Comparison of the fidelity between the initial state and the time-evolved state obtained from the original time-dependent Hamiltonian (solid lines) and from the effective Floquet Hamiltonian $\hat{H}^F$ (dashed lines). Panels (b) and (c) show the fidelity at the fixed evolution time $t = 10T$ for different values of θ, with $\omega_d = 1$ in (b) and $\omega_d = 5$ in (c). Panels (d) and (e) show the fidelity for the fixed initial angle $\theta = \pi/4$ at different evolution times $t = nT$, with $\omega_d = 1$ in (d) and $\omega_d = 5$ in (e). In all panels, the system size is $L = 12$.

In Fig. 7(a), we report the spectrum of the effective Floquet Hamiltonian $\hat{H}^F = \sum_m \tilde{\epsilon}^F_m |\tilde{\epsilon}^F_m\rangle \langle\tilde{\epsilon}^F_m|$ as a function of the driving amplitude h. The spectrum exhibits a characteristic candylike structure arising from the modulation by the Bessel function $J_0(h/\omega_d)$. The periodic narrowing of the spectrum corresponds to values of h for which the overall bandwidth is strongly reduced, leading to an abrupt slowdown of the dynamics.

We now numerically assess the validity of the effective description and identify the regimes in which it accurately reproduces the dynamics. We show that they provide an excellent approximation in the parameter regime considered in the main text, while they break down when the high-amplitude and high-frequency conditions are no longer satisfied. To this end, we compare the stroboscopic dynamics generated by the original time-dependent Hamiltonian $|\psi(nT)\rangle =$

$\hat{\mathcal{U}}(nT,0)\,|\psi(0)\rangle$ with those generated by the effective Floquet Hamiltonian $|\tilde{\psi}(nT)\rangle = \exp(-i\hat{H}^F nT)\,|\psi(0)\rangle$ by evaluating the corresponding revival probabilities $|\langle\psi(0)|\psi(nT)\rangle|^2$ and $|\langle\psi(0)|\tilde{\psi}(nT)\rangle|^2$, shown in Figs. 7(b)–7(e).

Specifically, we consider two driving frequencies: $\omega_d = 5$, corresponding to the regime investigated in the main text, and $\omega_d = 1$, which is comparable with Ω. The panels are organized following the same structure as Figs. 5(b) and 5(d). We first fix the evolution time to $t = 10T$ and compare the revival probability for different values of θ and then fix the initial angle to $\theta = \pi/4$ and compare the revival probability at different stroboscopic times $t = nT$. For both values of ω_d, we consider driving amplitudes h lying below the first FSN region.

In general, we observe that, for $\omega_d = 1$, the original and effective dynamics strongly disagree, while for $\omega_d = 5$, they show good agreement. Importantly, $\omega_d = 5$ is the driving frequency considered throughout the main text, and the agreement observed here confirms that the effective Floquet description is reliable in the parameter regime investigated in the paper. Indeed, for this value of ω_d, the conditions required for the validity of the effective Hamiltonian are satisfied: When $h \gg \tilde{\Omega} = 1/2$ (with energies expressed in units of Ω), the system is in the high-amplitude regime, while for values of h comparable with $\tilde{\Omega}$, one has $\omega_d \gg h, \tilde{\Omega}$, corresponding to the high-frequency regime. Therefore, for the range of parameters considered in the main text, at least one of the two regimes ensuring the validity of the Floquet description is fulfilled. Conversely, for $\omega_d = 1$, the driving frequency is always comparable with $\tilde{\Omega}$, so the high-frequency condition is not satisfied. Moreover, since we restrict to values of h before the first FSN region, h never becomes much larger than $\tilde{\Omega}$, and the high-amplitude regime is not reached either.

APPENDIX B: EFFECT OF THE SYSTEM SIZE ON THE FLOQUET SPECTRUM

In this Appendix, we provide a more comprehensive analysis of the dependence of the Floquet spectrum on the system size, going beyond the results presented in Fig. 2(a) and extending the behavior of n_{rev} shown in Fig. 3(e) to the full spectrum. In Fig. 8, we display the Floquet quasienergy spectrum as a function of the driving amplitude for several system sizes L.

As expected, increasing L leads to a progressively denser spectrum, reflecting the exponential growth of the Hilbert space and the corresponding increase in the number of states within the FBZ. Despite this densification, the overall qualitative structure of the spectrum, characterized by its distinctive candylike pattern, remains robust and essentially unaffected by system size. This indicates that the underlying organization of the Floquet eigenstates is stable against scaling.

From a quantitative perspective, we observe that the Floquet bandwidth grows with L, signaling that the extremal quasienergies spread over a wider range as the system size increases. In contrast, the dominant level spacing remains largely insensitive to L, see Fig. 3(e). This separation of scales highlights a key feature of the spectrum: While the global energy window expands, the local structure associated with nonthermal states is preserved.

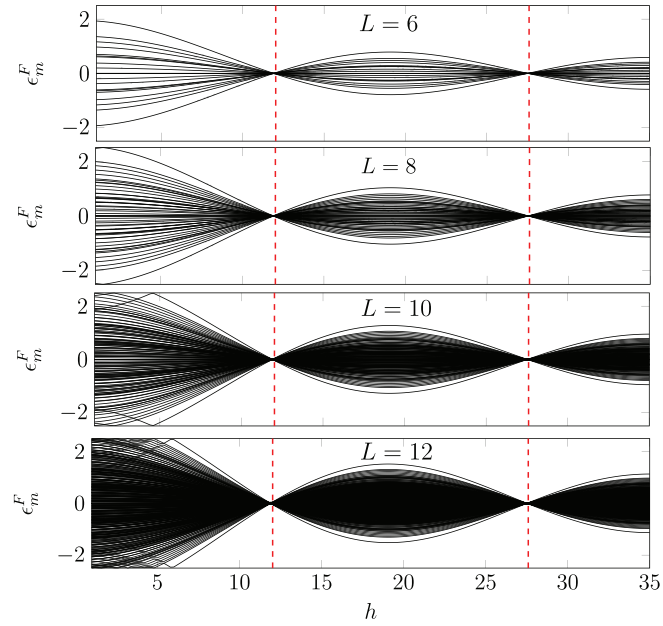


FIG. 8. Floquet spectrum as a function of the driving amplitude h for different values of the size L with $\omega_d = 5$. The vertical dashed red lines indicate the first two zeros of the $J_0(h/\omega_d)$ Bessel function: $h/\omega_d \approx 2.4048,\ 5.5201$.

This behavior closely parallels what is observed in the static PXP model, where the bandwidth increases with system size, yet the characteristic spacing between scarred eigenstates remains approximately constant.

APPENDIX C: ANALYSIS OF THE EXPECTED REVIVAL TIME

In this Appendix, we analyze in detail the behavior of n_{rev}, paying attention to its dependence on h for different values of ω_d. We focus on the region of driving parameters such that $h/\omega_d < 2.4048$. Assuming that the Floquet bandwidth follows $J_0(h/\omega_d)$ and that the dominant quasienergy spacing $\Delta\epsilon^F$ deforms proportionally to the bandwidth, we may posit that $\Delta\epsilon^F = \delta\, J_0(h/\omega_d)$, where δ is a proportionality factor, implying a direct proportionality between $\Delta\epsilon^F$ and the Bessel function. This, in turn, would naturally lead to $n_{\text{rev}} = \omega_d/[\delta\, J_0(h/\omega_d)]$. However, as we will show, this assumption is not completely accurate. In fact, fixing ω_d and inspecting the Floquet spectrum, we observe that, as shown in Fig. 2(a), for small h/ω_d, the spectrum is not shaped by the Bessel function $J_0(h/\omega_d)$, making the simple proportionality ansatz inaccurate. For this reason, we assume that the behavior is corrected by an offset and write

$$n_{\text{rev}}(h) = \frac{\omega_d}{\gamma J_0(h/\omega_d)} + \alpha. \tag{C1}$$

For $h \ll \omega_d$, we have $J_0(h/\omega_d) \approx 1$, so $n_{\text{rev}} \approx \frac{\omega_d}{\gamma} + \alpha$, while when approaching the FSN, we have $\frac{\omega_d}{\gamma J_0(h/\omega_d)} \gg \alpha$, leading to $n_{\text{rev}} \approx \frac{\omega_d}{\gamma J_0(h/\omega_d)}$. In the latter regime, the hypothetical validity of the fit confirms the correspondence between the deformation of the Floquet spectrum and the deformation of the dominant quasienergy spacing. In Figs. 9(a) and 9(b),

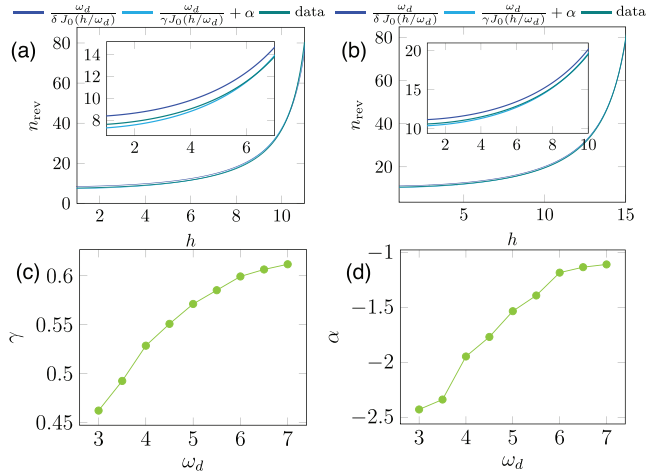


FIG. 9. (a) and (b) Comparison between n_{rev} extracted from the Floquet spectrum (data) and two different fits $\frac{\omega_d}{\gamma J_0(h/\omega_d)} + \alpha$ and $\frac{\omega_d}{\delta J_0(h/\omega_d)}$. Panel (a) shows the results for $\omega_d = 5$, while panel (b) shows the results for $\omega_d = 7$. The system size is fixed to $L = 10$ in both panels. (c) and (d) Fit parameters γ and α as a function of ω_d, obtained by fitting $n_{\text{rev}} = \frac{\omega_d}{\gamma J_0(h/\omega_d)} + \alpha$. The size of the system is $L = 10$.

we compare the behavior of $n_{\text{rev}}(h)$ for two fixed values of ω_d with the two proposed fits. In both cases, we observe that the fit given by Eq. (C1) works reasonably well, especially at small h. Consequently, we consider fixed values of $\omega_d \in [3, 3.5, 4, \ldots, 7]$, and for each ω_d, we fit $n_{\text{rev}}(h)$ data in the interval $h \in [1, 2.2048\omega_d]$, i.e., before the first zero of the Bessel function. The two fit parameters are plotted in Figs. 9(c) and 9(d) as a function of ω_d and are reported with their respective errors in Table I. Overall, the fit works better for larger ω_d, with the errors on the parameters decreasing accordingly. At the same time, the two fit parameters tend to stabilize for large ω_d. Finally, we note that this approach allows us to approximately identify the minimal time required

TABLE I. Fit parameters γ and α for different driving frequencies ω_d, with their respective uncertainties.

ω_d	γ	α
3	$0.462\,15 \pm 0.0116$	$-2.428\,85 \pm 0.4577$
3.5	$0.492\,468 \pm 0.003\,34$	$-2.338\,42 \pm 0.1314$
4	$0.528\,536 \pm 0.002\,67$	$-1.946\,13 \pm 0.1045$
4.5	$0.550\,855 \pm 0.002\,316$	$-1.768\,02 \pm 0.096\,38$
5	$0.571\,21 \pm 0.001\,885$	$-1.533\,36 \pm 0.080\,17$
5.5	$0.585\,289 \pm 0.001\,609$	$-1.390\,35 \pm 0.071\,79$
6	$0.599\,358 \pm 0.001\,26$	$-1.182\,18 \pm 0.056\,04$
6.5	$0.606\,491 \pm 0.001\,15$	$-1.132\,46 \pm 0.054\,98$
7	$0.611\,822 \pm 0.001\,078$	$-1.107\,51 \pm 0.055\,69$

for observing a revival at each ω_d. Indeed, since n_{rev} is a positive monotonically increasing function of h in the region of parameters considered, the minimal revival time is obtained for $J_0(h/\omega_d) \approx 1$, giving $n_{\text{rev}}^{\min} \approx \frac{\omega_d}{\gamma} + \alpha$. For instance, for $\omega_d = 7$, we have $n_{\text{rev}}^{\min} \approx 10.3325$.

APPENDIX D: EVALUATION OF Z_j^{erg}

Thermalizing driven closed quantum systems are characterized by long-time expectation values of local operators that coincide with those of the infinite-temperature mixed state. In the constrained Hilbert space of dimension $D_L = F_{L+2}$, this state reads

$$\hat{\rho}^{\text{erg}}_{[1,\ldots,L]} = \frac{\hat{\mathbb{1}}_{F_{L+2}}}{F_{L+2}} = \frac{1}{D_L} \sum_{\mathbf{s}\in\mathcal{B}_L} |\mathbf{s}\rangle_{[1,\ldots,L]} \langle \mathbf{s}| \,, \tag{D1}$$

where $\mathcal{B}_L$ denotes the constrained Hilbert space, and the subscript $[1, \ldots, L]$ indicates that the state is defined over the entire chain. In general, the subscript $[\ell_1, \ldots, \ell_2]$ specifies that the state has support on the region between sites ℓ_1 and ℓ_2 of the chain. This ergodic state can be decomposed recursively as

$$\hat{\rho}^{\text{erg}}_{[1,\ldots,L]} = \frac{1}{D_L} \sum_{\mathbf{s}\in\mathcal{B}_L} |\mathbf{s}\rangle_{[1,\ldots,L]} \langle \mathbf{s}| = \frac{1}{D_L} \left(|0\rangle_1 \langle 0| \otimes \sum_{\mathbf{s}\in\mathcal{B}_{L-1}} |\mathbf{s}\rangle_{[2,\ldots,L]} \langle \mathbf{s}| + |10\rangle_{[1,2]} \langle 10| \otimes \sum_{\mathbf{s}\in\mathcal{B}_{L-2}} |\mathbf{s}\rangle_{[3,\ldots,L]} \langle \mathbf{s}| \right), \tag{D2}$$

which using $D_L = F_{L+2}$, can be rewritten as

$$\hat{\rho}^{\text{erg}}_{[1,\ldots,L]} = \frac{F_{L+1}}{F_{L+2}} |0\rangle_1 \langle 0| \otimes \hat{\rho}^{\text{erg}}_{[2,\ldots,L]} + \frac{F_L}{F_{L+2}} |10\rangle_{[1,2]} \langle 10| \otimes \hat{\rho}^{\text{erg}}_{[3,\ldots,L]}. \tag{D3}$$

By tracing out sites $[2, \ldots, L]$, we obtain the reduced state of the first site

$$\left(\hat{\rho}^{\text{erg}}_{[1,\ldots,L]}\right)_1 := \text{Tr}_{[2,\ldots,L]} \left[\hat{\rho}^{\text{erg}}_{[1,\ldots,L]}\right] = \frac{F_{L+1}}{F_{L+2}} |0\rangle \langle 0| + \frac{F_L}{F_{L+2}} |1\rangle \langle 1| \,. \tag{D4}$$

For simplicity, we denote the reduced state $(\hat{\rho}^{\text{erg}}_{[1,\ldots,L]})_j$ as $\hat{\rho}^{\text{erg}}_j$.

The same reasoning can be applied recursively to the second site, yielding

$$\begin{aligned} \hat{\rho}^{\text{erg}}_{[1,\ldots,L]} &= \frac{1}{D_L} \left[(|0\rangle_1 \langle 0| + |1\rangle_1 \langle 1|) \otimes |0\rangle_2 \langle 0| \otimes \sum_{\mathbf{s}\in\mathcal{B}_{L-2}} |\mathbf{s}\rangle_{[3,\ldots,L]} \langle \mathbf{s}| + |010\rangle_{[1,2,3]} \langle 010| \otimes \sum_{\mathbf{s}\in\mathcal{B}_{L-3}} |\mathbf{s}\rangle_{[4,\ldots,L]} \langle \mathbf{s}| \right] \\ &= \frac{1}{F_{L+2}} \left[F_L \left(|10\rangle_{[1,2]} \langle 10| \otimes \hat{\rho}^{\text{erg}}_{[3,\ldots,L]} + |00\rangle_{[1,2]} \langle 00| \otimes \hat{\rho}^{\text{erg}}_{[3,\ldots,L]} \right) + F_{L-1} (|010\rangle_{[1,2,3]} \langle 010| \otimes \hat{\rho}^{\text{erg}}_{[4,\ldots,L]} \right], \end{aligned} \tag{D5}$$

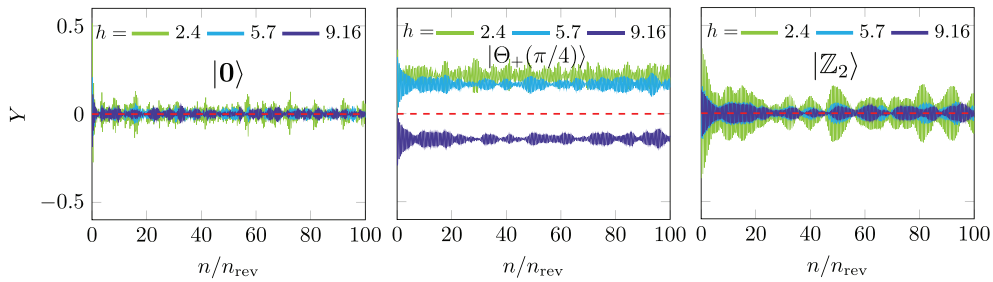


FIG. 10. Analysis of the long-time dynamics of $Y(t)$ for different initial states $[|\mathbf{0}\rangle\,,\ |\Theta_+(\pi/4)\rangle\,,\ |\mathbb{Z}_2\rangle]$ and different driving amplitude values; the latter are $h = 2.4, 5.7, 9.14$ and have revival times that are approximately integer multiples of the period $n_{\rm rev} = \omega_d/\Delta\epsilon^F \approx 8, 11, 25$. The driving frequency is fixed to $\omega_d = 5$ and $L = 12$.

and so

$$\hat{\rho}_2^{\rm erg} = \frac{2F_L}{F_{L+2}}\,|0\rangle\langle 0| + \frac{F_{L-1}}{F_{L+2}}\,|1\rangle\langle 1|\,. \tag{D6}$$

More generally, for a site j in the bulk, the full ergodic state can be expressed as

$$\hat{\rho}^{\rm erg}_{[1,\ldots,L]} = \frac{1}{D_L}\Bigg[\left(\sum_{\mathbf{s}\in\mathcal{B}_{j-1}} |\mathbf{s}\rangle_{[1,\ldots,j-1]}\langle\mathbf{s}|\right)\otimes|0\rangle_j\langle 0|\otimes\left(\sum_{\mathbf{s}\in\mathcal{B}_{L-j}}|\mathbf{s}\rangle_{[j+1,\ldots,L]}\langle\mathbf{s}|\right) + \left(\sum_{\mathbf{s}\in\mathcal{B}_{j-2}}|\mathbf{s}\rangle_{[1,\ldots,j-2]}\langle\mathbf{s}|\right)\otimes|010\rangle_{[j-1,j,j+1]}\langle 010|\otimes\left(\sum_{\mathbf{s}\in\mathcal{B}_{L-j-1}}|\mathbf{s}\rangle_{[j+2,\ldots,L]}\langle\mathbf{s}|\right)\Bigg]. \tag{D7}$$

Taking the partial trace over all sites except j gives the general site-reduced ergodic state

$$\hat{\rho}_j^{\rm erg} = \frac{F_{j+1}F_{L-j+2}}{F_{L+2}}\,|0\rangle\langle 0| + \frac{F_jF_{L-j+1}}{F_{L+2}}\,|1\rangle\langle 1|\,. \tag{D8}$$

Using $F_1 = F_2 = 1$ and $F_3 = 2$, one can verify that this expression holds for any site j in the chain. This result implies that the ergodic expectation value of $\hat{Z}_j$ reads

$$Z_j^{\rm erg} = {\rm Tr}\left[\hat{\rho}_j^{\rm erg}\hat{Z}_j\right] = \frac{F_jF_{L-j+1} - F_{j+1}F_{L-j+2}}{F_{L+2}}. \tag{D9}$$

From the diagonal structure of $\hat{\rho}_j^{\rm erg}$, it immediately follows that $X_j^{\rm erg} = Y_j^{\rm erg} = 0$.

APPENDIX E: LONG-TIME DYNAMICS OF Y

In this Appendix, we report and briefly discuss the dynamics of the Y operator. Following the discussion in the main text, Sec. VI, Fig. 10 shows the dynamics for three different initial states (different panels) and three values of the driving field h (different colors), with ω_d fixed.

The results reveal three distinct long-time dynamical regimes. For a system initialized in the polarized state, Y weakly and noisily fluctuates around the ergodic expectation value, while for the Néel state, it exhibits more coherent oscillations. In contrast, the interpolating state $|\Theta_+(\pi/4)\rangle$ displays oscillations far from the ergodic value, with a strong dependence on h.

[1] I. M. Georgescu, S. Ashhab, and F. Nori, Quantum simulation, Rev. Mod. Phys. **86**, 153 (2014).

[2] A. J. Daley, I. Bloch, C. Kokail, S. Flannigan, N. Pearson, M. Troyer, and P. Zoller, Practical quantum advantage in quantum simulation, Nature (London) **607**, 667 (2022).

[3] A. Browaeys and T. Lahaye, Many-body physics with individually controlled Rydberg atoms, Nat. Phys. **16**, 132 (2020).

[4] A. Aspuru-Guzik and P. Walther, Photonic quantum simulators, Nat. Phys. **8**, 285 (2012).

[5] E. Altman *et al.*, Quantum simulators: Architectures and opportunities, PRX Quantum **2**, 017003 (2021).

[6] L. Amico *et al.*, Roadmap on atomtronics: State of the art and perspective, AVS Quantum Sci. **3**, 039201 (2021).

[7] J. Polo, W. J. Chetcuti, E. C. Domanti, P. Kitson, A. Osterloh, F. Perciavalle, V. P. Singh, and L. Amico, Perspective on new implementations of atomtronic circuits, Quantum Sci. Technol. **9**, 030501 (2024).

[8] O. Morsch, G. M. Palma, and D. Rossini, Quantum simulations of complex systems, Riv. Nuovo Cimento **48**, 275 (2025).

[9] J. Polo, W. Chetcuti, T. Haug, A. Minguzzi, K. Wright, and L. Amico, Persistent currents in ultracold gases, Phys. Rep. **1137**, 1 (2025).

[10] L. D'Alessio and M. Rigol, Long-time behavior of isolated periodically driven interacting lattice systems, Phys. Rev. X **4**, 041048 (2014).

[11] M. Rigol, V. Dunjko, and M. Olshanii, Thermalization and its mechanism for generic isolated quantum systems, Nature (London) **452**, 854 (2008).

[12] M. Srednicki, Chaos and quantum thermalization, Phys. Rev. E **50**, 888 (1994).

[13] H. Bernien, S. Schwartz, A. Keesling, H. Levine, A. Omran, H. Pichler, S. Choi, A. S. Zibrov, M. Endres, M. Greiner, *et al.*, Probing many-body dynamics on a 51-atom quantum simulator, Nature (London) **551**, 579 (2017).

[14] C. J. Turner, A. A. Michailidis, D. A. Abanin, M. Serbyn, and Z. Papić, Quantum scarred eigenstates in a Rydberg atom chain: Entanglement, breakdown of thermalization, and stability to perturbations, Phys. Rev. B **98**, 155134 (2018).

[15] A. Pal and D. A. Huse, Many-body localization phase transition, Phys. Rev. B **82**, 174411 (2010).

[16] L. Capizzi, J. Wang, X. Xu, L. Mazza, and D. Poletti, Hydrodynamics and the eigenstate thermalization hypothesis, Phys. Rev. X **15**, 011059 (2025).

[17] A. M. Kaufman, M. E. Tai, A. Lukin, M. Rispoli, R. Schittko, P. M. Preiss, and M. Greiner, Quantum thermalization through entanglement in an isolated many-body system, Science **353**, 794 (2016).

[18] J. Smith, A. Lee, P. Richerme, B. Neyenhuis, P. W. Hess, P. Hauke, M. Heyl, D. A. Huse, and C. Monroe, Many-body localization in a quantum simulator with programmable random disorder, Nat. Phys. **12**, 907 (2016).

[19] I. Lesanovsky and H. Katsura, Interacting Fibonacci anyons in a Rydberg gas, Phys. Rev. A **86**, 041601(R) (2012).

[20] W. W. Ho, S. Choi, H. Pichler, and M. D. Lukin, Periodic orbits, entanglement, and quantum many-body scars in constrained models: Matrix product state approach, Phys. Rev. Lett. **122**, 040603 (2019).

[21] M. Serbyn, D. A. Abanin, and Z. Papić, Quantum many-body scars and weak breaking of ergodicity, Nat. Phys. **17**, 675 (2021).

[22] A. Hudomal, J.-Y. Desaules, B. Mukherjee, G.-X. Su, J. C. Halimeh, and Z. Papić, Driving quantum many-body scars in the PXP model, Phys. Rev. B **106**, 104302 (2022).

[23] A. Chandran, T. Iadecola, V. Khemani, and R. Moessner, Quantum many-body scars: A quasiparticle perspective, Annu. Rev. Condens. Matter Phys. **14**, 443 (2023).

[24] S. Choi, C. J. Turner, H. Pichler, W. W. Ho, A. A. Michailidis, Z. Papić, M. Serbyn, M. D. Lukin, and D. A. Abanin, Emergent SU(2) dynamics and perfect quantum many-body scars, Phys. Rev. Lett. **122**, 220603 (2019).

[25] A. Lerose, T. Parolini, R. Fazio, D. A. Abanin, and S. Pappalardi, Theory of robust quantum many-body scars in long-range interacting systems, Phys. Rev. X **15**, 011020 (2025).

[26] J.-Y. Desaules, F. Pietracaprina, Z. Papić, J. Goold, and S. Pappalardi, Extensive multipartite entanglement from SU(2) quantum many-body scars, Phys. Rev. Lett. **129**, 020601 (2022).

[27] A. Kerschbaumer, M. Ljubotina, M. Serbyn, and J.-Y. Desaules, Quantum many-body scars beyond the PXP model in Rydberg simulators, Phys. Rev. Lett. **134**, 160401 (2025).

[28] A. Daniel, A. Hallam, J.-Y. Desaules, A. Hudomal, G.-X. Su, J. C. Halimeh, and Z. Papić, Bridging quantum criticality via many-body scarring, Phys. Rev. B **107**, 235108 (2023).

[29] A. Pizzi, L.-H. Kwan, B. Evrard, C. B. Dag, and J. Knolle, Genuine quantum scars in many-body spin systems, Nat. Commun. **16**, 6722 (2025).

[30] F. Perciavalle, G. M. Rizzo, F. Plastina, and N. L. Gullo, Local reminiscence in the PXP model, arXiv:2509.19944.

[31] A. Banerjee, Quantum scarring enhances non-Markovianity of subsystem dynamics New J. Phys. **28**, 054502 (2026).

[32] F. M. Surace, M. Votto, E. G. Lazo, A. Silva, M. Dalmonte, and G. Giudici, Exact many-body scars and their stability in constrained quantum chains, Phys. Rev. B **103**, 104302 (2021).

[33] A. Eckardt and E. Anisimovas, High-frequency approximation for periodically driven quantum systems from a Floquet-space perspective, New J. Phys. **17**, 093039 (2015).

[34] G. E. Santoro, *Introduction to Floquet Theory*, Lecture Notes (SISSA, Trieste, 2019).

[35] A. Russomanno, *Periodic Driving of a Coherent Quantum Many Body System and Relaxation to the Floquet Diagonal Ensemble*, Ph.D. thesis, Scuola Internazionale Superiore di Studi Avanzati (SISSA), Trieste, 2014.

[36] E. C. Domanti, D. Zappalà, A. Bermudez, and L. Amico, Floquet-Rydberg quantum simulator for confinement in $\mathbb{Z}_2$ gauge theories, Phys. Rev. Res. **6**, L022059 (2024).

[37] S. Geier, N. Thaicharoen, C. Hainaut, T. Franz, A. Salzinger, A. Tebben, D. Grimshandl, G. Zürn, and M. Weidemüller, Floquet Hamiltonian engineering of an isolated many-body spin system, Science **374**, 1149 (2021).

[38] M. Sato and T. N. Ikeda, Floquet theory and applications in open quantum and classical systems, J. Phys. Soc. Jpn. **94**, 111007 (2025).

[39] M. Holthaus, Floquet engineering with quasienergy bands of periodically driven optical lattices, J. Phys. B: At. Mol. Opt. Phys. **49**, 013001 (2016).

[40] S. Lorenzo, J. Marino, F. Plastina, G. M. Palma, and T. J. G. Apollaro, Quantum critical scaling under periodic driving, Sci. Rep. **7**, 5672 (2017).

[41] D. Bluvstein, A. Omran, H. Levine, A. Keesling, G. Semeghini, S. Ebadi, T. T. Wang, A. A. Michailidis, N. Maskara, W. W. Ho, *et al.*, Controlling quantum many-body dynamics in driven Rydberg atom arrays, Science **371**, 1355 (2021).

[42] P. Dutta, S. Choudhury, and V. Shukla, Prethermalization in the PXP model under continuous quasiperiodic driving, Phys. Rev. B **111**, 064303 (2025).

[43] H. K. Park and S. Lee, Subharmonic fidelity revival in a driven PXP model, Phys. Rev. B **107**, 205142 (2023).

[44] P. Dutta, K. L. Panigrahi, and V. Shukla, Controlling quantum scars and engineering subharmonic responses with a two frequency drive, arXiv:2508.12809.

[45] L.-Z. Tang, X. Li, Z. D. Wang, and D.-W. Zhang, Discrete time crystals enabled by Floquet strong Hilbert space fragmentation, Phys. Rev. B **113**, 214303 (2026).

[46] N. Maskara, A. A. Michailidis, W. W. Ho, D. Bluvstein, S. Choi, M. D. Lukin, and M. Serbyn, Discrete time-crystalline order enabled by quantum many-body scars: Entanglement steering via periodic driving, Phys. Rev. Lett. **127**, 090602 (2021).

[47] W. Deng and Z.-C. Yang, Using models with static quantum many-body scars to generate time-crystalline behavior under periodic driving, Phys. Rev. B **108**, 205129 (2023).

[48] X. Luo, Y. Zhou, Z. Xu, and W. Jiang, Discrete time quasicrystal in Rydberg atomic chain, arXiv:2505.09117.

[49] A. Haldar, R. Moessner, and A. Das, Onset of Floquet thermalization, Phys. Rev. B **97**, 245122 (2018).

[50] L. Staszewski, A. Haldar, P. W. Claeys, and A. Wietek, Krylov space dynamics of ergodic and dynamically frozen Floquet systems, arXiv:2510.19824.

[51] K. Seetharam, P. Titum, M. Kolodrubetz, and G. Refael, Absence of thermalization in finite isolated interacting Floquet systems, Phys. Rev. B **97**, 014311 (2018).

[52] Y. Hou, A. Pizzi, H. Jin, J. Knolle, R. Moessner, and H. Zhao, Floquet superheating, arXiv:2511.12877.

[53] G. Giudici, F. M. Surace, and H. Pichler, Unraveling PXP many-body scars through Floquet dynamics, Phys. Rev. Lett. **133**, 190404 (2024).

[54] B. Mukherjee, S. Nandy, A. Sen, D. Sen, and K. Sengupta, Collapse and revival of quantum many-body scars via Floquet engineering, Phys. Rev. B **101**, 245107 (2020).

[55] K. Mizuta, K. Takasan, and N. Kawakami, Exact Floquet quantum many-body scars under Rydberg blockade, Phys. Rev. Res. **2**, 033284 (2020).

[56] X. Liang, Z. Yue, Y.-X. Chao, Z.-X. Hua, Y. Lin, M. K. Tey, and L. You, Observation of anomalous information scrambling in a Rydberg atom array, Phys. Rev. Lett. **135**, 050201 (2025).

[57] A. Haldar, D. Sen, R. Moessner, and A. Das, Dynamical freezing and scar points in strongly driven Floquet matter: Resonance vs emergent conservation laws, Phys. Rev. X **11**, 021008 (2021).

[58] A. Lazarides, A. Das, and R. Moessner, Equilibrium states of generic quantum systems subject to periodic driving, Phys. Rev. E **90**, 012110 (2014).

[59] T. Mori, T. N. Ikeda, E. Kaminishi, and M. Ueda, Thermalization and prethermalization in isolated quantum systems: A theoretical overview, J. Phys. B: At. Mol. Opt. Phys. **51**, 112001 (2018).

[60] M. C. Bañuls, J. I. Cirac, and M. B. Hastings, Strong and weak thermalization of infinite nonintegrable quantum systems, Phys. Rev. Lett. **106**, 050405 (2011).

[61] S. Krämer, D. Plankensteiner, L. Ostermann, and H. Ritsch, QUANTUMOPTICS.JL: A Julia framework for simulating open quantum systems, Comput. Phys. Commun. **227**, 109 (2018).